

Passive control of vortex-shedding past finite cylinders under the effect of a free surface

Cite as: Phys. Fluids 35, 015109 (2023); <https://doi.org/10.1063/5.0134730>

Submitted: 13 November 2022 • Accepted: 14 December 2022 • Accepted Manuscript Online: 15 December 2022 • Published Online: 05 January 2023

 I. A. Carvalho and  G. R. S. Assi



[View Online](#)



[Export Citation](#)



[CrossMark](#)

ARTICLES YOU MAY BE INTERESTED IN

Direct numerical simulation of flow over a cylinder immersed in the grid-generated turbulence
Physics of Fluids **34**, 015109 (2022); <https://doi.org/10.1063/5.0072730>

DeepTRNet: Time-resolved reconstruction of flow around a circular cylinder via spatiotemporal deep neural networks

Physics of Fluids **35**, 015118 (2023); <https://doi.org/10.1063/5.0129049>

Evolution and control of multiscale vortical structures in a wall-mounted cube wake

Physics of Fluids **35**, 015128 (2023); <https://doi.org/10.1063/5.0132761>



Physics of Fluids

Special Topic: Paint and Coating Physics

Submit Today!

Passive control of vortex-shedding past finite cylinders under the effect of a free surface

Cite as: Phys. Fluids 35, 015109 (2023); doi: 10.1063/5.0134730

Submitted: 13 November 2022 · Accepted: 14 December 2022 ·

Published Online: 5 January 2023



View Online



Export Citation



CrossMark

I. A. Carvalho^{1,a)} and G. R. S. Assi^{2,b)}

AFFILIATIONS

¹Department of Mechanical Engineering, EPUSP, University of São Paulo, São Paulo, Brazil

²Department of Naval Architecture & Ocean Engineering, EPUSP, University of São Paulo, São Paulo, Brazil

^{a)}Author to whom correspondence should be addressed: amorim.icaro@usp.br

^{b)}Electronic mail: g.assi@usp.br

ABSTRACT

Passive technologies for the control of the flow past bluff bodies have been widely studied. Most of these works have focused on high-aspect-ratio, wall-mounted, or infinitely long cylinders, leaving a gap for low-aspect-ratio bodies fully submerged or under the effect of a free water surface. This is the object of the present work. Detached-eddy simulations at a Reynolds number of 1000 have been carried out for infinitely long (case i) and low-aspect-ratio bodies. For the finite case, two configurations were investigated: bodies fully submerged in the flow, away from surface effects (case ii) and that involving a free surface, here represented by a fixed slip-allowing plane (case iii). These computations were conducted for the bare cylinder and the system is comprised of the same main body fitted with eight wake-control rods uniformly distributed around its perimeter. Results showed that the low-aspect-ratio cases relative to infinitely long structures (1) lowered mean drag and root mean square lift, (2) presented a less coherent wake topology, (3) had frontal rods that concentrated most of the hydrodynamic loads, (4) extended the formation length, and (5) although all cases developed larger hydrodynamic loads when the rods were fitted to the main body compared to the plain cylinder, the finite cases produced a lower increase. We show that these results are intrinsically related to end effects and associated with a less correlated wake lacking coherent vortical structures. Furthermore, we analyze the more accentuated streamwise vortices produced by the presence of the free surface in case iii compared with case ii.

Published under an exclusive license by AIP Publishing. <https://doi.org/10.1063/5.0134730>

I. INTRODUCTION

Vortex shedding is responsible for cyclic hydrodynamic loads that affect bluff structures. The interplay between opposing vortices shed downstream is the root of vortex-induced vibrations (VIV) that cause the bluff structure to oscillate longitudinally, and principally, transversely to the flow, leading to fatigue and possibly failure. In practice, VIV (sometimes also called VIM for vortex-induced motion of large floating structures) is observed in large offshore platforms with bluff hulls, such as spar and monocolumn platforms. The present study is a part of a research line to develop devices to suppress VIV of floating offshore structures. Knowledge of the physical mechanisms obtained from numerical simulations should help the development of active and passive technologies to control the flow around bluff bodies.

Various methods to eliminate or attenuate vortex shedding have been reviewed by Zdravkovich (1981) and Choi *et al.* (2008). Passive solutions aim at suppressing VIV without any power input. Common examples are shrouds (such as slender cylinders around the main body), near-wake stabilizers (such as end plates and splitter plates),

and complex geometrical modifications [like helical strakes recently studied by Assi *et al.* (2022)].

From a physical point of view, this passive category of solutions acts through different mechanisms. One such is through the elimination or delay of vortex shedding farther downstream in the wake, thus diffusing vorticity. It is known from the classic work of Gerrard (1966) that shear layers feed the wake with vorticity and their interaction is of utmost relevance to the shedding mechanism. Hence, other strategies will try to avoid shear layer interaction.

From the seminal paper on the suppression of vortex shedding by a single control rod of Strykowski and Sreenivasan (1990), it is known that the presence of a passive secondary body can attenuate the growth of temporal instabilities and is able to not only reduce vortex shedding but also banish its inception entirely in a limited range of Reynolds numbers ($Re = U_\infty D / \nu$, where U_∞ is the freestream flow velocity, D is the diameter of the main body, and ν is the kinematic viscosity of the fluid). In a more general sense, numerical and experimental results of Strykowski and Sreenivasan (1990) for Re

comprehended between 40 and 100 showed that local modifications led to global changes in the flow and that in order to control the wake, interaction with the near field is of vital importance.

Experiments with more complex systems subjected to VIV were conducted by Silva-Ortega and Assi (2017; 2018), with 2, 4, and 8 rods in turbulent regime. Drag and response amplitude were assessed regarding changes in the gap between the main body and the fitted rods and their diameters. The authors showed that care must be taken with such a passive device, which may not only increase hydrodynamic loads but also introduce galloping due to directional effects. With an adequate choice of parameters, only residual vibration due to VIV remained for a setup involving eight control rods.

Generally, most of the previous works were concerned with flow control over infinitely long cylinders, in which the end effects were neglected. Relatively, few works were dedicated to the flow behavior past finite cylinders even though the subject dates back to experiments made one century ago by Wieselsberger (1922).

Farivar (1981) experimentally studied the turbulent flow at $Re = 7 \times 10^4$ about cylinders with finite length of different aspect ratios. Supported by the work of Goldstein (1965) on the turbulent flow about a cylinder with different aspect ratios, Farivar (1981) attempted to describe the effect of the free end regarding pressure and drag coefficients. Franzini *et al.* (2013) studied the problem of a bare cylinder subjected to VIV for aspect ratios in the range of 0.3–2.0 and different mass ratios and also reported the lack of studies of cylinders with small aspect ratios. The study of Gonçalves *et al.* (2015) advanced on the matter and evaluated the flow around stationary circular cylinders piercing through the water surface for very low aspect ratios, ranging from $L/D = 0.1$ to 2.0.

Major contributions on finite cylinders are found in the scope of wall-mounted setups. In one of the early works, Kawamura *et al.* (1984) experimentally detected the existence of trailing vortices and downwash and their relation to the formation of the Kármán vortex street. The authors noted that depending on the slenderness parameter L/D (where L is the length of the cylinder), this wake could not form. Rather, for sufficient L/D , the trailing vortices dominated the wake. Later, Luo (1993) pointed out that the formation of a Kármán vortex street for finite cylinders depended on a critical value of the aspect ratio L/D that ranged between 1 and 7 depending on the influence of the plane boundary layer. Working with different L/D , Sumner *et al.* (2004) produced time-averaged velocity and streamwise vorticity contours that showed tip-vortex structures, near-wake recirculations, and

downwash. It was also found that the effect of the tip vortices extended into the wake downstream and scaled with the cylinder length. The authors also reported that a coherent Kármán vortex street was not observed for $L/D < 3$. Instead, a symmetric “arch-vortex” dominated the near wake.

Both active and passive solutions have been employed in 2D laminar cases and three-dimensional (3D) fully turbulent cases. Still, there is a lack of research concerning both mechanisms for finite cylinders subjected to end effects. It was remarked by Mittal and Raghuvanshi (2001) that the suppression of vortex shedding (in infinitely long cylinders) by proper placement of a fixed rod near the main cylinder was possible only at low Re . Nevertheless, wake control by a passive mechanism is a stepping stone toward more effective solutions, such as active control through the injection of momentum into the boundary layer by spinning the rods (Korkischko and Meneghini, 2012; Assi *et al.*, 2019). The review of Luo *et al.* (1996) is one of the few studies that evaluated the flow interaction between low aspect ratio cylinders; however, the authors were not concerned with a passive mechanism as described above. Rather, the focus was given to the interference between two bodies of sizes of the same order.

As it can be seen, although the problem of the flow past finite cylinders has been explored, particularly for the wall-mounted setup, in general, it is still scarcer in information than that of infinitely long bodies as already anticipated in the work of Sumner *et al.* (2004). At present, no analysis has been made modeling the free surface as a slip surface with a system like the one we propose in this work. Furthermore, fitted rods to the main body have not been employed as a form of passive mechanism of finite bluff bodies.

II. OBJECTIVE

In the present paper, we intend to push forward the literature on the matter of passive control of finite structures by studying free-surface and free-end effects on the vortex shedding mechanism and its suppression with interfering rods. We compare the flow behavior over infinitely long and low-aspect-ratio cylinders.

Configurations of the flow past a plain cylinder and past a system—that involves the main body fitted with peripheral rods—have been considered. The motivation to fit the rods around the main body is to investigate how the entire set [as illustrated in Fig. 1(a)] interacts with the near wake to control vortex shedding. In the scope of finite cylinders, two setups have been studied: one in which the

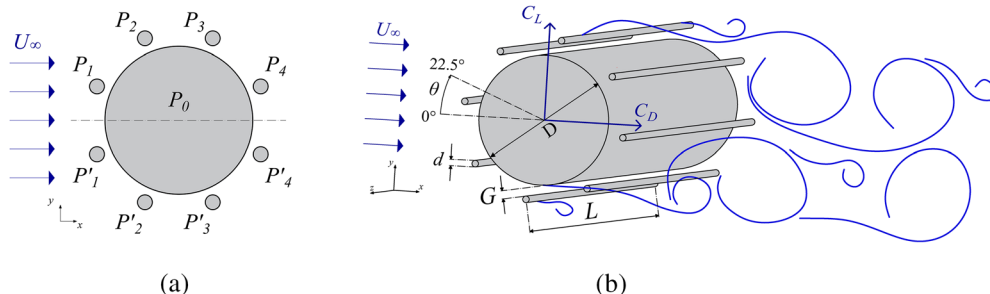


FIG. 1. (a) System comprised of the main cylinder (P_0) and eight rods P_1, P_2, P_3, P_4 and their primed counterparts, symmetrically displayed with respect to the x -axis crossing the center of the system. (The figure is not to scale for better visualization.) (b) Parameters of the flow and the system formed by the main cylinder and the eight fitted peripheral rods.

system was fully submerged with two free ends and another in which a free surface was attached to one of the ends.

Results from the numerical simulations performed at $Re = 1000$ will be discussed in terms of hydrodynamic loads, wake topology, and wake interaction with the free surface and free-end effects.

III. METHODOLOGY

A. Problem description

The incoming uniform flow with flow speed U_∞ was set past a plain cylinder of diameter D and past a system comprised of the main cylinder (P_0) surrounded by eight peripheral rods (P_n). Figure 1(b) represents the aforementioned system, showing the central body surrounded by eight fixed rods of diameter $d = D/20$. A gap $G = D/100$ was set between the walls of the main cylinder and the rods. This geometry has been deeply studied in other works with and without spinning rods (Assi *et al.*, 2019; Carvalho *et al.*, 2021; Carvalho and Assi, 2022).

It should be noted that designated frontal and rear rods were deliberately displaced away from the stagnation regions of the main body by an angle of 22.5° . In addition, rods were evenly distributed along a circumference of radius $D/2 + G + d/2$ centered at the origin of the entire system (coincident with the center of the main body) apart from one another by 45° .

Regarding the end conditions of the cylinders, three cases have been investigated (shown in Fig. 2):

Case i, infinitely long body: The periodic boundary conditions in the numerical domain guaranteed that no end effects would interfere with the three-dimensional flow, thus producing an infinitely long body (Fig. 2, left).

The next cases employed finite bodies with three-dimensional end effect. A low aspect ratio of $L/D = 2$ was set for all simulations:

Case ii, finite body, fully submerged: Both free ends of the low-aspect-ratio cylinder were exposed to three-dimensional flow. The boundaries of the numerical domain were set sufficiently far apart not to interfere with the flow around the body (Fig. 2, middle).

Case iii, finite body with a free surface: One of the free ends of the cylinder was replaced by a free surface, modeled here as a plane that allowed free slipping of the flow (Fig. 2, right). A two-phase flow has not been considered.

Finally, regarding possible wave interactions on a real free surface, we verified that the Froude number based on the cylinder's length

(given by $Fr = U_\infty / \sqrt{gL}$, where g is the gravitational acceleration) was inferior to 0.23. According to Newman (2018), for a subcritical regime of $Fr < 1$, the wave pattern is similar to that expected for deep waters. Generally, for $Fr < 0.5$, water elevation due to free surface effects is deemed negligible. Thus, since wave effects are not significant in the present study, our setup fits well in these conditions and the free surface can be adequately represented by a slip-allowing plane. Gonçalves *et al.* (2018), for example, employed a similar approach for an experimental investigation of floating bluff bodies in a water channel.

B. Finite volume scheme and meshing

The incompressible flow in a turbulent regime was simulated at a Reynolds number $Re = U_\infty D / \nu = 10^3$, based on the main cylinder's diameter D , incoming flow speed U_∞ , and fluid viscosity ν . Finite volume simulations were performed in OpenFOAM, an open-source C++ library, to obtain the second-order discretization of the governing equations of mass conservation and momentum transport for incompressible flow and Newtonian fluid, as given by the Navier-Stokes and continuity equations in the differential form below:

$$\rho \left(\frac{\partial U_i}{\partial t} + U_j \frac{\partial U_i}{\partial x_j} \right) = - \frac{\partial p}{\partial x_i} + \mu \frac{\partial^2 U_i}{\partial x_j \partial x_j}, \quad (1)$$

$$\frac{\partial U_j}{\partial x_j} = 0. \quad (2)$$

The left-hand side of the equation was discretized by means of an implicit backward scheme for the Eulerian term and with a second-order blend of the linear upwind and central scheme (with proportion 1:3) for the convective term. Gradients followed a cell-based least squares procedure. Linear interpolation allowed for the computations on the surface of the cells from cell center values. The discretization of the Laplacian term was attained by a surface-normal gradient corrected for non-orthogonality together with the Gauss theorem. All turbulent quantities were subjected to a linear upwind discretization. All terms followed a second-order truncation error.

Coupling between pressure and velocity was made with the transient version of the SIMPLE algorithm of Patankar (1980). This was necessary because there is not a transport equation for the pressure or an equation of state relating pressure and velocity, as it can be

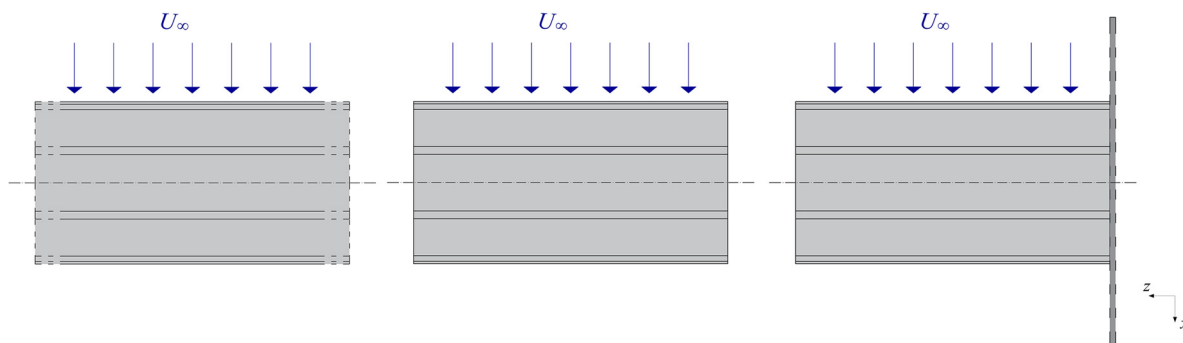


FIG. 2. Three cases regarding end effects: system with nominally infinite span, where end effects are neglected (left), fully immersed finite system (middle), and finite system under the effect of a free surface (right).

observed from Eqs. (1) and (2). For the velocity field, a tight tolerance of 10^{-8} was imposed for convergence of each time step. For pressure, the simulation of the bare cylinder of case i was simulated with maximum residual tolerance of 10^{-6} , while other cases adopted 10^{-4} . From Carvalho and Assi (2022), it became clear that this lower tolerance for the pressure did not compromise the results and yet allowed for faster simulations.

Symmetry boundary conditions (no flow across) were applied to the sides of the domain and the free surface of case iii, and no-slip condition was applied to the surfaces of the cylinders. The inflow was specified by the flow velocity U_∞ and zero pressure gradient; the outflow was set at a fixed pressure and null velocity gradient. Inlet and outlet are shown in Fig. 3, in which L_s and L_f represent the distances from the system ends to the sides of the domain.

Case i was reproduced by means of a spanwise length of the bodies $L = \pi D$ (in agreement with Assi *et al.*, 2018), accompanied by periodic boundary conditions on the sides of the domain to simulate the flow over infinitely long bodies. In this case, and using Fig. 3 as a reference, L_s and L_f were set to zero and the width of the domain matched the cylinders' span.

Finite bodies were specified with length $L = 2D$. The immersed bodies of case ii laid distant $L_s = L_f = 8D$ from the sides of the domain.

To simulate case iii—the flow about the bare cylinder and about the entire system with a free surface—one of the sides of the bodies was attached to one a slip surface (at $z = -D$), so, $L_f = 0$ and $L_s = 8D$ were imposed.

In any of these cases, the center of the main cylinder was distant $8D$ from the top and bottom surfaces and the inlet. A greater distance of $20D$ was applied between the main cylinder's center and the outlet downstream. These dimensions for the grid geometry corroborate with the work of Behr *et al.* (1995; 1991), Kim and Mohan (2005), and with Carvalho and Assi (2022)—where a wider domain of the same mesh was investigated—and are, thus, expected to mitigate blockage effects.

Hexahedral and prismatic elements covered the flow domain, and mesh refinement was conducted toward the bodies and in the wake region to capture typical gradients related to vortices and eddies. Away from the cylinders and the wake, the cells were made larger. Figure 4 portrays a cross-section passing through the system for the cases of infinitely long [Fig. 4(a)] and finite bodies [Fig. 4(b)]. (For reference, the set of axis is given in Fig. 3.)

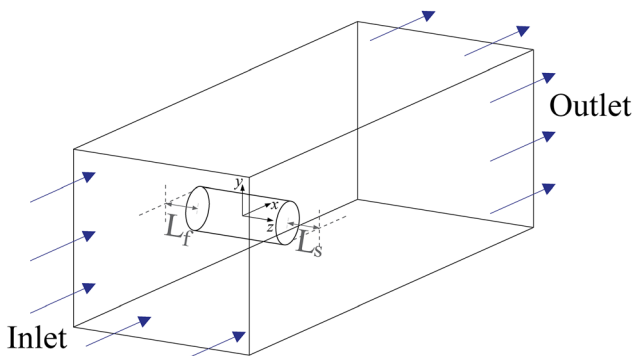
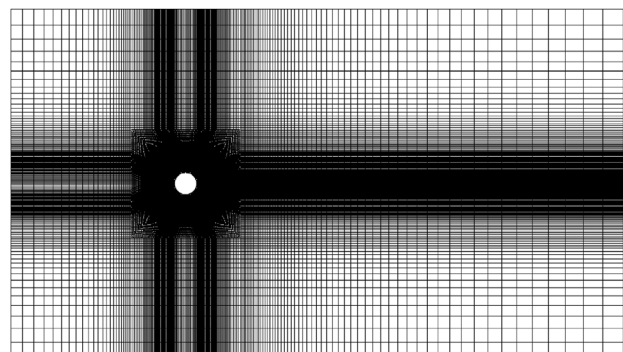
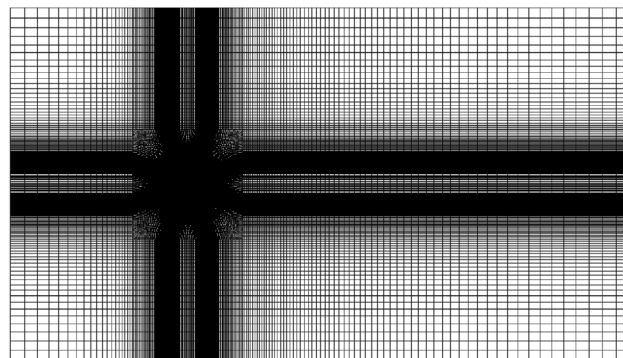


FIG. 3. Numerical domain. Only the main cylinder is represented for clarity.



(a) Case i.



(b) Cases ii and iii.

FIG. 4. Meshed domain of the system for cases i (a) and ii and iii (b) for a cross section (z -plane) passing through the system. The flow is in the x -direction. (a) Case i. (b) Cases ii and iii.

Exclusively structured and hexahedral elements were used for case i although they were also predominant in the other cases as well. In particular, this type of element was employed to capture boundary layer features. Unstructured, prismatic, elements composed of the cells located on the free ends of the cylinders of cases ii and iii, and the region extruded away to the sides from these surfaces. A planar view of rod P_1 is shown in Figs. 5(a) and 5(b), where triangular elements (of the yet non-extruded mesh) were employed on the free ends of the main cylinder and the rods. Figure 5(c) shows the same rod in a 3D spanwise view and captures its end fixed to the free surface.

For all three cases, the smallest element measured $10^{-3}D$ on the wall of the bare cylinder; for the configurations involving the entire system, it spanned $1.54 \times 10^{-3}D$ for the main body and $3.77 \times 10^{-3}D$ for the rods to ensure quality results near the boundary layer and dispense with wall functions. It must be taken into account that the rods were on the verge of vortex shedding because the Reynolds number based on their diameter $Re_d = Ud/\nu$ was merely 50.

Extrusion of the cases of infinitely long bodies and of the finite bodies are depicted in Fig. 6. For the case of infinitely long cylinders, Fig. 6(a) shows that uniform refinement was applied along the span of the bodies, and their free ends were disregarded. In contrast, the second case [Fig. 6(b)] was refined near the tips of the cylinders, which were closed by a side surface. In particular, this second figure shows

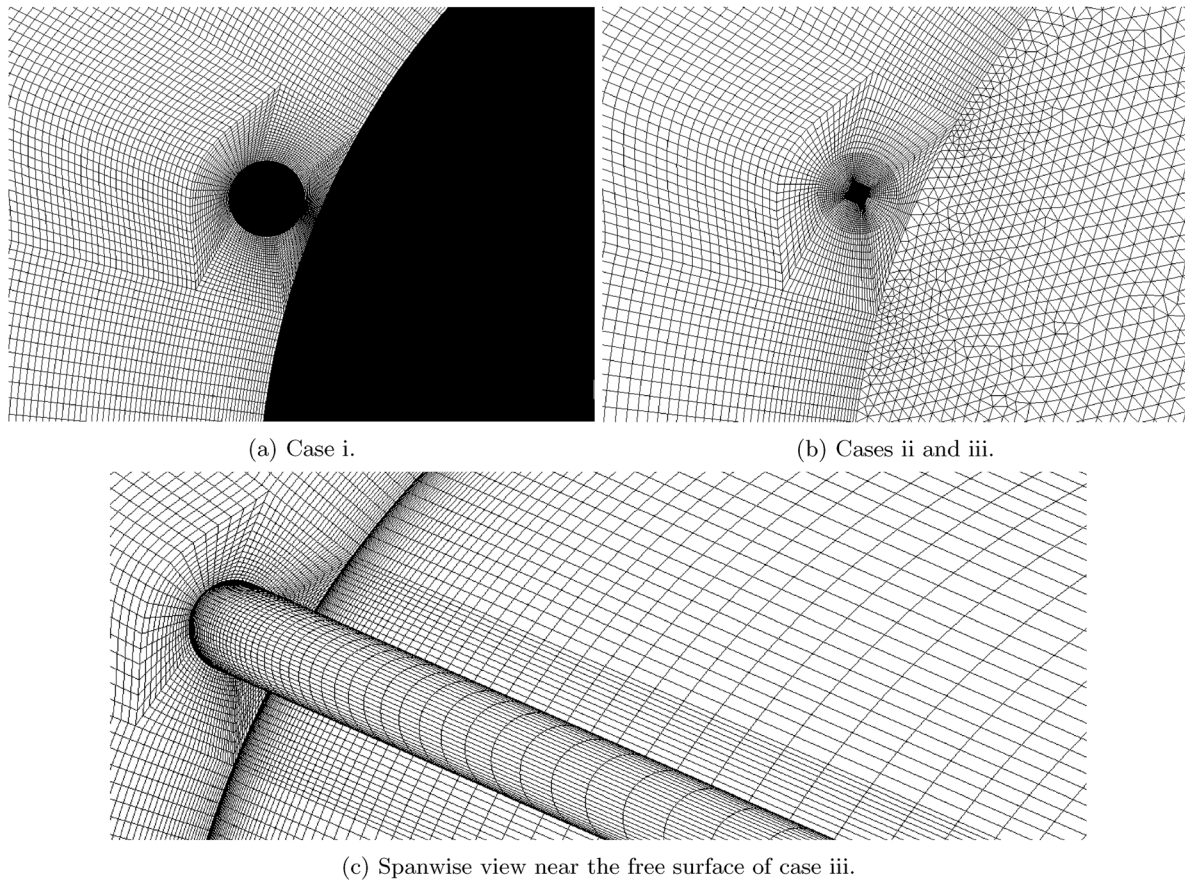


FIG. 5. Cross section of the meshes for cases i (a), ii and iii (b) showing rod P_1 . Grids used for the low-aspect ratio cases required meshing of every cylinder side to capture end effects (b). Spanwise refinement is captured in (c). (a) Case i. (b) Cases ii and iii. (c) Spanwise view near the free surface of case iii.

the triangular-shaped elements that comprised part of the lateral surface of the main cylinder.

C. Turbulence modeling

Note: This section details the approach to turbulence modeling employed in the present investigation, especially considering future works that might advance the numerical scheme. The non-specialized reader may skip this section without losing comprehension of the results.

For cost-effective 3D simulations involving turbulence scales, the detached-eddy simulation (DES) approach was elected (Spalart, 1997) together with the one-equation model of Spalart and Allmaras (1992) for the turbulent viscosity parameter $\tilde{\nu}$ within the resolution of the boundary layer involving such a Reynolds-averaged Navier–Stokes (RANS) model,

$$\frac{\partial \tilde{\nu}}{\partial t} + U_j \frac{\partial \tilde{\nu}}{\partial x_j} = c_{b1}(1 - f_{t2})\tilde{S}\tilde{\nu} + \frac{1}{\tilde{\sigma}} \left\{ \frac{\partial}{\partial x_k} \left[(\nu + \tilde{\nu}) \frac{\partial \tilde{\nu}}{\partial x_k} \right] + c_{b2} \frac{\partial \tilde{\nu}}{\partial x_k} \frac{\partial \tilde{\nu}}{\partial x_k} \right\} - \left(c_{w1}f_w - \frac{c_{b1}}{\kappa^2}f_{t2} \right) \left(\frac{\tilde{\nu}}{d_{wall}} \right)^2,$$

where the notation d_{wall} is the distance from the wall. Further constants were set as

$$\begin{aligned} \tilde{\sigma} &= 2/3, & \kappa &= 0.41, & c_{b1} &= 0.1355, & c_{b2} &= 0.622, & c_{w2} &= 0.3, \\ c_{w3} &= 2, & c_{v1} &= 7.1c_{w1} = c_{b1}/\kappa^2 + (1 + c_{b2})/\tilde{\sigma}, & c_{t3} &= 0, \\ c_{t4} &= 0.5. \end{aligned}$$

Among the following expressions, f_{t2} and f_w are damping functions:

$$\begin{aligned} \chi &= \tilde{\nu}/\nu, & f_{t2} &= c_{t3} \exp(-c_{t4}\chi^2), \\ f_{v1} &= \chi^3/(\chi^3 + c_{v1}^3), & f_{v2} &= 1 - \chi/(1 + \chi f_{v1}), \\ \tilde{S} &= \max \left\{ \left| \frac{\partial U_i}{\partial x_j} - \frac{\partial U_j}{\partial x_i} \right| + \frac{\tilde{\nu}}{\kappa^2 d_{wall}^2} f_{v2}, c_s \left(\frac{\partial U_i}{\partial x_j} - \frac{\partial U_j}{\partial x_i} \right) \right\}, \\ f_w &= g \left[\frac{(1 + c_{w3}^6)}{(g^6 + c_{w3}^6)} \right]^{1/6}, \\ g &= r + c_{w2}(r^6 - r), & r &= \min(\tilde{\nu}/\tilde{S}\kappa^2 d^2, 10). \end{aligned}$$

The relationship between the turbulent viscosity ν_t and the turbulent viscosity parameter $\tilde{\nu}$ was given by

$$\nu_t = \tilde{\nu} f_{v1}.$$

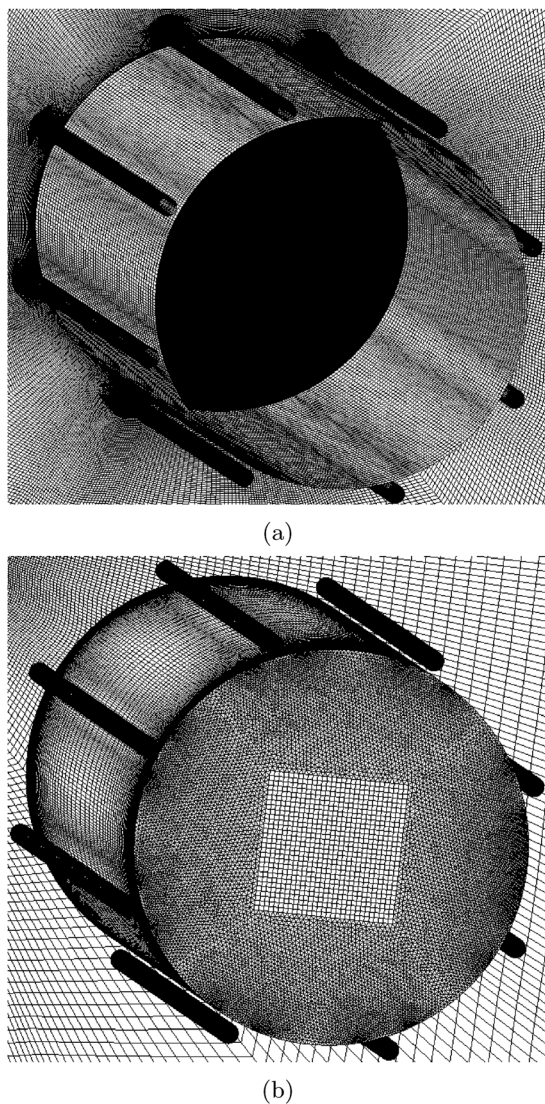


FIG. 6. Extruded meshes for both cases of infinitely long (a) and low-aspect-ratio cylinder (b). In the former, it is seen that spanwise mesh refinement is uniform, whereas refinement is enhanced near the ends of the cylinders for the latter.

A major problem in the DES formulation for the flow about cylindrical structures in a sub-critical regime is that the boundary layer is laminar, whereas the wake is already turbulent (Saltara *et al.*, 2011), and the RANS formulation for the boundary layer is intrinsically turbulent. This downside was circumvented by a low- Re correction (Ψ Spalart *et al.*, 2006)

$$\Psi = \min \left\{ 10^2, \left[1 - \frac{c_{b1}}{c_{w1} \kappa^2 f_w^*} (f_{l2} + (1-f_{l2})f_{v2}) \right] \times [f_{v1} \max(10^{-10}, 1-f_{l2})]^{-1} \right\}, \quad (3)$$

so the characteristic length of the DES formulation (l_{DES}) became

$$l_{DES} = \min(\Psi C_{DES} \Delta, d_{wall}),$$

where Δ is the largest dimension of the cell and the remaining calibrating constants are $C_{DES} = 0.65$ and $f_w^* = 0.424$. This approach was shown to work well in Carvalho and Assi (2022).

IV. RESULTS

A. Reference simulations

Reference simulations were carried out first for verification, validation, and grid independence test with respect to drag (C_D) and lift (C_L) coefficients, respectively, given by the corresponding loads non-dimensionalized by $\rho U^2 DL/2$. For case i, these results are found in Carvalho and Assi (2022) and will not be repeated here for brevity.

For case ii, validation was made with the results substantiated by Goldstein (1965) apud Farivar (1981) for cylinders of finite length, where the authors found that the mean drag was $\overline{C_D} = 0.67$ at $Re = 8.8 \times 10^4$ for an aspect ratio of 1.98. Our simulation at $Re = 10^4$ produced $\overline{C_D} = 0.64$, in agreement with Goldstein (1965) over 95.5%. We disclose that it is, indeed, a feature of this field that recent papers have hardly dealt with measurements over finite cylinders of low aspect ratio with both ends free or under the effect of a water surface. Most of the papers on this matter are from the past century. Recent results either take L/D much greater than 2 or consider another setup, such as wall-mounted bodies or stationary bodies piercing through the water surface.

Table I presents the grid independence test at $Re = 10^3$, in relation to mean drag ($\overline{C_D}$) and root mean square (RMS) lift (\hat{C}_L). The highlighted lines correspond to the meshes that will serve as references for cases ii and iii throughout the text. Most quantities showed variance below 10%, thus presenting good convergence, except for the RMS lift coefficient of case iii. However, this greater variance was to be expected for \hat{C}_L of this case as these are small quantities and strongly vary, even after taking a simulation time that spanned $40T_S$ as it was done here. We remark that T_S is the time span of a vortex shedding cycle in the case of the flow past an infinitely long bare cylinder in a subcritical regime.

To further confirm the quality of our meshing, we have verified the convergence of the mean pressure coefficient ($\overline{C_p}$) of case iii. This

TABLE I. Grid independence test with respect to mean drag ($\overline{C_D}$) and RMS lift (\hat{C}_L) for cases ii and iii. The highlighted rows show variance below 10% relative to the most refined mesh hereby tested, except for \hat{C}_L of case iii, thus providing a good compromise between computational resources and accuracy.

Number of cells	Bare cylinder			
	Case ii (finite)		Case iii (free surface)	
	$\overline{C_D}$	\hat{C}_L	$\overline{C_D}$	\hat{C}_L
4 466 680	0.71	0.0414	3 385 152	0.72
6 679 440	0.69	0.0708	4 107 512	0.72
8 433 710	0.69	0.0338	4 829 872	0.73
10 198 560	0.68	0.0380	5 552 232	0.73
12 322 680	0.68	0.0330	6 274 592	0.72
15 293 080	0.69	0.0330	8 257 368	0.72

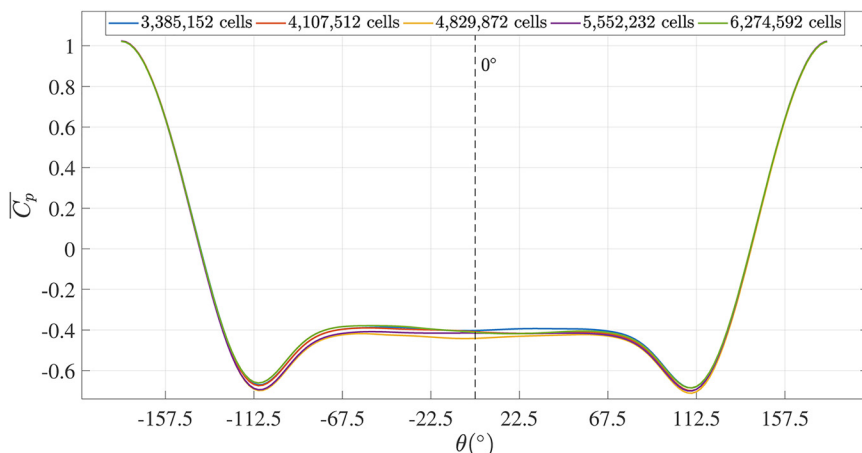


FIG. 7. Case iii mesh convergence study. Mean pressure coefficients \bar{C}_p were taken at different angular positions at $z = L/D$.

analysis was conducted over the circumference of the bare cylinder at different $\theta = \tan^{-1}(y/x)$ angles at $z = L/D$, and it is given in Fig. 7. From the figure, it becomes clear that no significant difference can be ascertained about the mean pressure coefficient among the different levels of mesh refinement.

We note that the mesh used for the system with finite bodies here followed precisely that for the infinitely long system of Carvalho *et al.* (2021) in the same turbulent Re -regime and Carvalho and Assi (2022) in the laminar regime, in the sense that the latter structured mesh was merely extruded along the span of the cylinder with refinement toward the tips. About 102 cells described the span of the finite cylinders and 100 represented the flow domain away from the tips (in the spanwise z -direction) of every side. Due to the unstructured mesh applied to the side faces of the cylinders (see Fig. 6), the extruded mesh departing from them was unstructured as well, as it can be visualized by Fig. 4. In total, 30 997 904 and 19 153 204 cells were, correspondingly, used for the entire system of cases ii and iii encompassing prismatic and hexahedral elements altogether.

Finite bodies' simulations require large meshes for adequate representation of the flow. For a cost-effective grid independence study of such systems, only the grid of case iii was assessed. Of course, mesh-wise, this case also incorporated the stencil features of case ii with respect to the immersed end of the system. Thus, this analysis allowed us to investigate both the convergence of cases ii and iii at once. $40T_S$ were run for each simulation and only the last $20T_S$ were used for the computation of mean and RMS quantities. The grids were constrained to the same size $D/1000$ of the first element near the wall for a fair comparison. Mean drag and RMS lift are presented in Table II. In parenthesis, the percentile difference relative to the reference mesh is given. For the mean drag, the difference between the meshes was below 3%. For lift, the discrepancy was generally greater the coarser the mesh. Still, the table shows that all values were in the same order of magnitude; considering that \hat{C}_L was given by a low value, larger deviance was expected in mesh convergence.

We selected the most refined mesh (highlighted in Table II) to represent the flow about a finite system with a free surface. For case ii, basically, the same mesh was used. The only difference was that the region where there is a free surface in case iii was replaced by an immersed end in case ii (with a symmetrical mesh to that of the

immersed end of case iii), thus justifying our mesh convergence procedure.

B. Time histories of hydrodynamic loads

All simulations were left to run for $15T_S$, assumed to be part of the numerical transient that preceded converged and realistic physical results. After this, in order to compute mean and RMS quantities, the simulations spanned at least another 25 additional cycles of vortex shedding, resulting in a total run of at least $40T_S$. T_S here is based on the common assumption that, in agreement with experiments, the Strouhal number can be reasonably approximated by $S_t = (T_S/D/U)^{-1} \approx 0.2$ for an infinitely long fixed cylinder in the sub-critical regime, as it can be noted from the compiled results of Norberg (2001).

Thick and thin lines in Fig. 8 correspond to the $25T_S$ converged time histories of lift and drag, respectively. It can be clearly noted that infinitely long cylinders led to the most accentuated hydrodynamic loads and frequency of vortex shedding among the different cases. In any case, the entire system produced greater loads than the plain cylinder. Additionally, attaching a free surface to one end of the cylinders, as in case iii, caused the mean drag to increase compared to the fully immersed system of case ii, see Table III.

A dampening of shedding frequencies is strikingly evident in Fig. 8 for both the setups of a plain cylinder and the entire system in cases

TABLE II. Grid independence test with respect to mean drag (\bar{C}_D) and RMS lift (\hat{C}_L) for the entire system of case iii.

Entire system (case iii)		
Number of cells	\bar{C}_D	\hat{C}_L
19 153 204	1.02	0.035
12 017 194	1.02	0.030
9 648 254	0.994	0.033
7 273 476	0.998	0.027
5 372 486	1.00	0.020

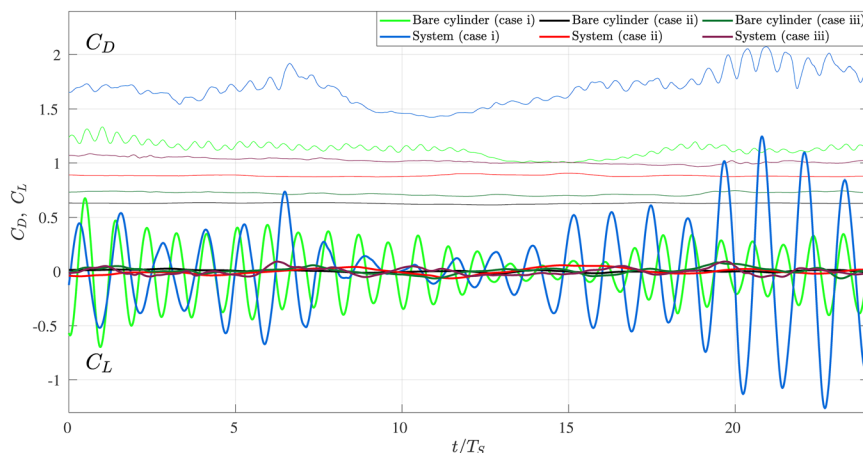


FIG. 8. Converged time histories of lift and drag. The time has been nondimensionalized by the duration of a vortex-shedding cycle. Thick lines correspond to measurements of lift; thin lines correspond to drag.

ii and iii against case i, followed by their much lower mean coefficients. From $\overline{C_D}$ curves, visual inspection indicates progressive flattening of the fluctuations on the order of cases i, iii, and ii, which is the same order as that where end effects were subsequently incorporated into the system configuration. In case i, end effects were not accounted for; in case iii, only one end was free (as the other was attached to the free surface), and in case ii, both ends interacted with the flow.

Because the bare cylinder presented lower \hat{C}_L than the entire system for any corresponding case (see Table III), a lift increase can be regarded as a consequence of attaching the slender rods to the main body.

C. Vorticity contours

Comparing the setup of the bare cylinder with that of the entire system, the more pronounced drag in the latter might be explained by the relatively greater low-pressure region downstream of the system, produced by the wider wake as revealed by Fig. 9. The figure also shows a less coherent distribution of vortical content within the wake of the finite cases ii and iii that lowered mean drag compared with that of case i, as described below in Sec. IV E.

For case i, the wider wake was accompanied by stronger and larger opposing vortices (first row of Fig. 9) whose response on the structure was translated into greater transversal loads. For cases ii and iii, higher lift due to the presence of the rods is explained by the fact that a wider wake and anticipated roll-up of the shear layers resulted from the presence of the rods (second row of Fig. 9). Of course, vortices are stronger, the nearer they are to the separation point of the shear layer, which acts as their source of vorticity (Gerrard, 1966). As the

diffused vortices were shed more distant from the body, the viscosity of the fluid continuously dissipated their strength (from Tennekes and Lumley, 1972, we recall that viscous shear is proportional to velocity gradients, a major feature of the vortices).

Figure 10 supports this argument through Q -contours of high and low levels of vorticity (red and translucent blue-colored), which are evidently associated with small and large coherent vortices, respectively. Turbulent structures carrying high vorticity in case i were ubiquitous and led to a wider wake. The other cases presented weaker vorticity levels and overall more concentrated Q -contours within the shorter wake. From Kawamura *et al.* (1984), for the present L/D value, indeed, the wake was expected to be narrower in finite cases. However, different from these authors, our case involved the interaction of two trailing vortices from the ends of the cylinders instead of that between a trailing vortex (from one free end) and a “necklace vortex” (from the other, wall-mounted, end).

Indeed, the formation length was prolonged by 7.2%, 6.7%, and 12.4% for cases i, ii, and iii, respectively, as the result of the insertion of the rods around the main body, see Fig. 11. We recall that the formation length is defined as the distance from the body to “that point downstream of the body where the velocity fluctuation level has grown to a maximum (and thereafter decays downstream)” (Williamson, 1996). These results are supported by the contours of the time-averaged squared fluctuation of the velocity, as shown in Fig. 12, where the wider wake is highlighted by the enlargement of the spacing between the shear layers detached from the sides (white lines). We note that the boundary and the shear layers were obtained as white contours which corresponded to $0.99U_\infty$, thus justifying the recurrent appearance of the white curve even before the system or, as in case iii, away from the bodies. In the latter, following contours of $0.99U_\infty$, we can note that the wake recovered faster the velocity of the incoming flow past the obstruction of the bodies in comparison with case ii.

It is also worth mentioning that the asymmetry (relative to $x=0$, see Fig. 3) found in the contours of Fig. 12 derived inherently from the randomness of the turbulent flow. This becomes more evident from comparing the subfigure of the bare cylinder of case i against the other cases. The asymmetry reveals clearer either as a result of end effects (as it will be explored below) or due to the increased complexity of the turbulent flow structures due to the addition of the rods.

TABLE III. Mean and RMS coefficients.

Case	Bare cylinder		Entire system	
	$\overline{C_D}$	\hat{C}_L	$\overline{C_D}$	\hat{C}_L
i	1.13	0.233	1.71	0.464
ii	0.631	0.0113	0.883	0.0303
iii	0.722	0.0325	1.020	0.0347

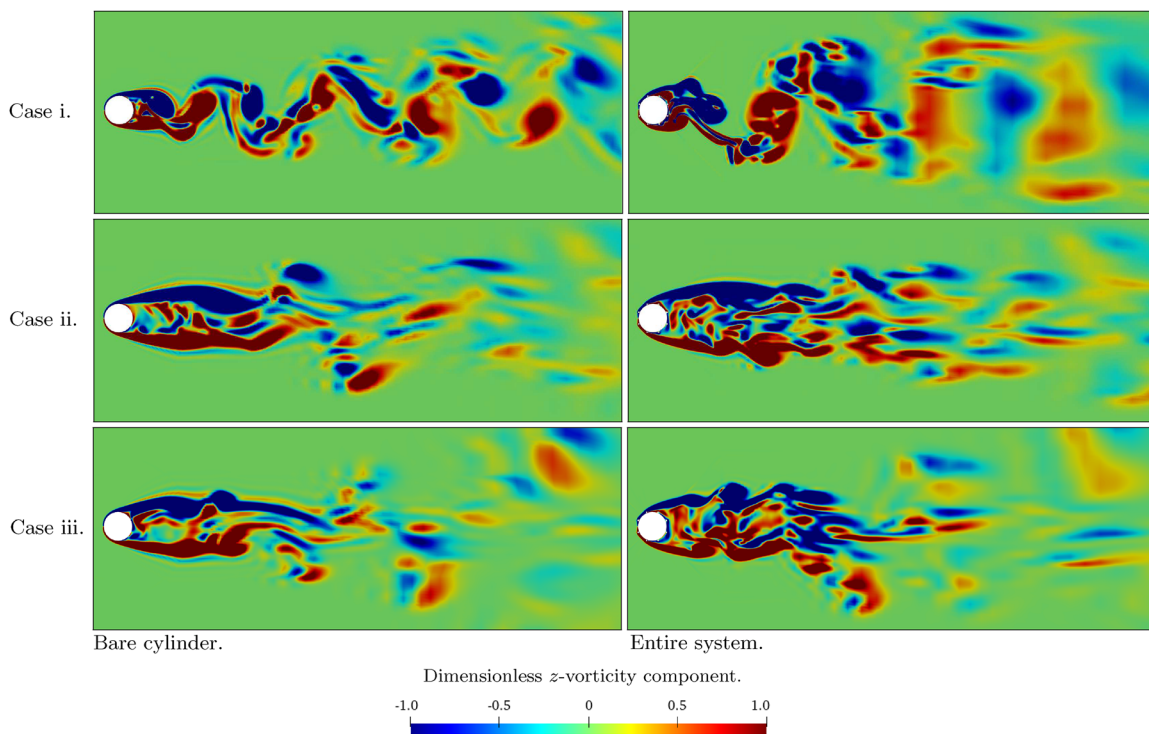


FIG. 9. Dimensionless z -vorticity component, scaled by U_∞/D . Finite cases correspond to the cross-section midway along the cylinders' span. All cases were taken at a positive peak of the lift curve.

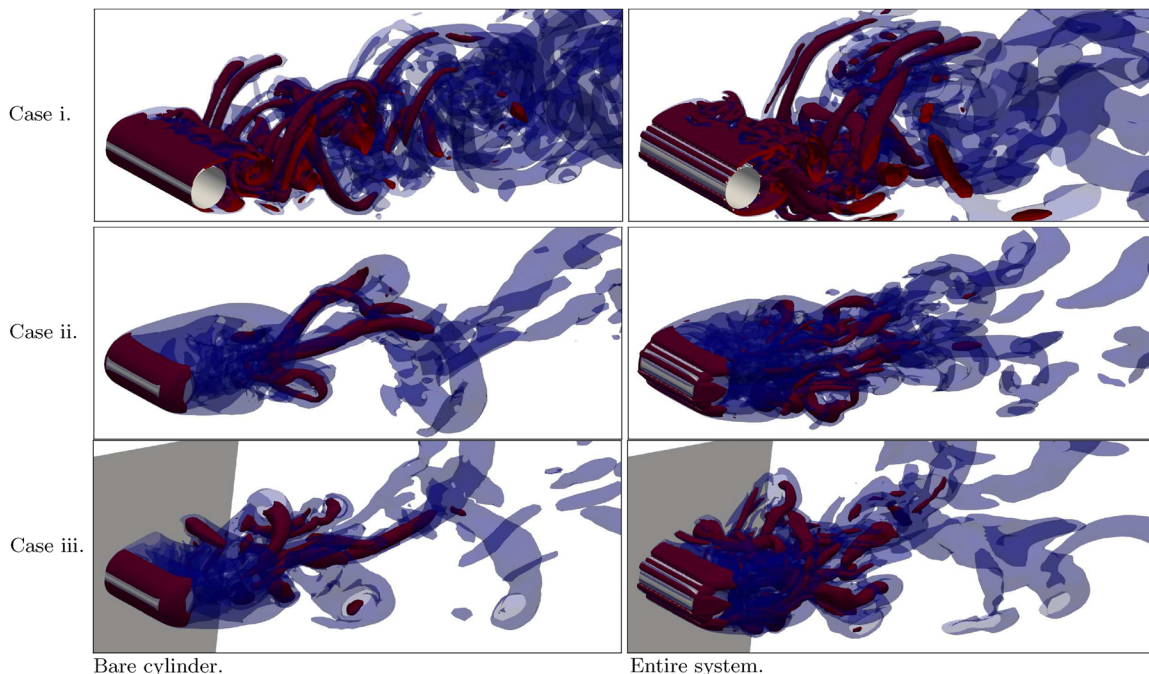


FIG. 10. Q-contours of high and low vorticity at $Q = 2.5$ (red) and $Q = 0.1$ (blue, transparent), respectively. The plain cylinder case is located on the left and the entire system on the right. For ease of visualization, only part of the plane corresponding to the free surface is shown (in gray).

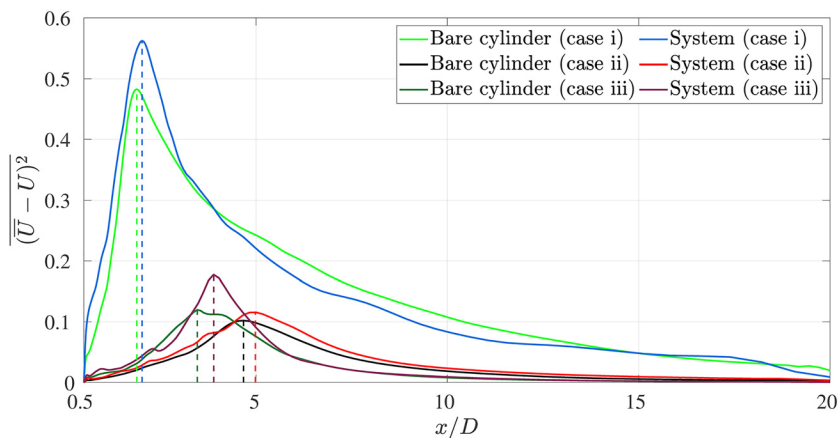


FIG. 11. Increase of mean formation length as the result of fitting the slender rods to the main body. The formation length is marked by x/D , where the mean fluctuation of the velocity was at peak value (abscissae of the dashed lines).

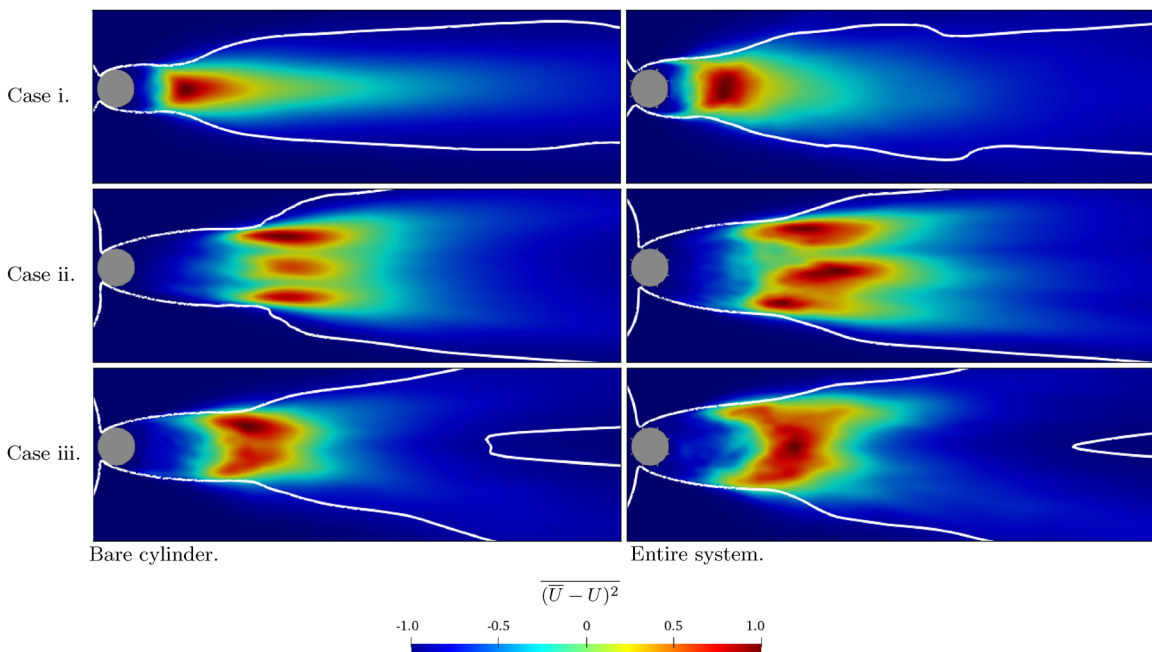


FIG. 12. Contours of the time-averaged square of the mean velocity fluctuations for cases i (top), case ii (middle), and case iii (bottom row) on the plane $z = 0$. The distance from the posterior stagnation point on the system to the location of maximum mean fluctuation defines the formation length.

D. Hydrodynamic loads on each cylinder

One important measure is that of hydrodynamic loads on the main body P_0 to which the passive mechanism was installed. Measurements of mean drag and RMS lift highlight that in case i, changing from the bare cylinder to the entire system increased mean drag by 43.3% and RMS lift by 63.6% for the main body. In case ii, the respective changes were 31.7% and 134%. In case iii, mean drag and RMS lift changed by 33.0% and -5.85% . The actual amounts are provided in Table IV for reference.

TABLE IV. Hydrodynamic coefficients.

Case	Bare cylinder		P_0	
	$\overline{C_D}$	\hat{C}_L	$\overline{C_D}$	\hat{C}_L
i	1.13	0.233	1.61	0.381
ii	0.631	0.0113	0.826	0.0265
iii	0.722	0.0325	0.960	0.0306

In terms of drag, a relative reduction of at least 40.4% was observed for the mean drag of P_0 for the passive mechanism in finite cylinders against its equivalent effect in the infinitely long setup. This can generally be attributed to three-dimensional effects, mainly to the disruption of the greater correlation in wake of the infinitely long case against the finite cases.

On the matter of lift changes, the explanation is less obvious. For case i, the analysis converges to that of Carvalho and Assi (2022), i.e., stronger vortices, a wider wake and more correlated structures along the spanwise direction of the system (due to the assumption of infinitely long cylinders) led to higher RMS lift. For cases ii and iii, similar effects were present, in addition to trailing edge effects as explained in Sec. IV E.

Figures 13(a) and 13(b) show mean drag and lift coefficients that acted on each individual rod, according to their angular positions [refer to Fig. 1(b)]. Rods P_2 , P'_2 were subjected to the greater absolute reduction in $\overline{C_D}$ and $\overline{C_L}$ of all rods. Contrarily, rods P_3 , P'_3 seemed oblivious to the different approaches. Rods P_1 , P'_1 experienced an increase in $\overline{C_D}$ from null value and a decrease in $|\overline{C_L}|$ (with emphasis on case ii for both loads) and P_4 , P'_4 shifted with opposite tendencies toward negligible contribution. This is in agreement with Carvalho et al. (2021); Carvalho and Assi (2022) in the sense that P_2 , P'_2 exceeded the other rods in relevance, as measured by the magnitude of the forces acting on it. In addition, this symmetric set of passive elements was demonstrated to be more sensitive among the different cases than the other rods. Contrary to the aforementioned papers,

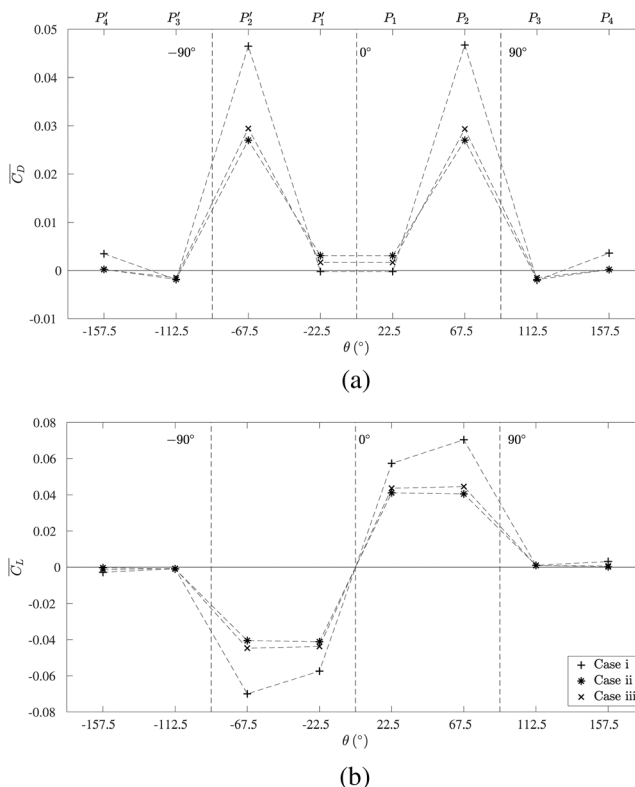


FIG. 13. Mean drag (a) and RMS lift (b) on each of the control rods for both cases of infinitely long cylinders and that of the low aspect ratio (finite cylinders).

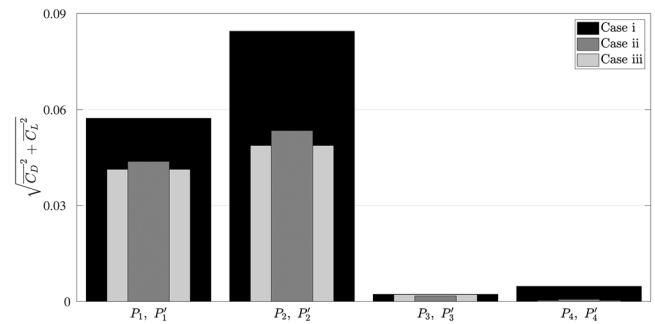


FIG. 14. Total force upon the upper rods of the entire system. By symmetry, their counterparts were subjected to the same loads. Among the different cases, it stands out compared with the previous works that P_4, P'_4 presented negligible loads in finite cases ii and iii compared with the infinitely long case i.

P_1 , P'_1 did not carry a negligible mean drag load although it was lower than P_2 , P'_2 .

The negligible influence of P_4 in Fig. 14 stands out (by symmetry, this applies to P'_4 as well). The previous studies (Assi et al., 2019; Carvalho et al., 2021; Carvalho and Assi, 2022) with infinite cylinders showed that within the scope of a passive mechanism, P_3 , P'_3 were affected with lower forces. Here, the opposite is seen. As the rods were modeled finite, P_3 , P'_3 remained comparable within cases i, ii, and iii, but, P_4 , P'_4 became apparently irrelevant in the latter two cases against the infinitely long case. This draws attention to how these curves would compare with an active mechanism, where all rods would spin to promote the reattachment of the boundary layer, as it was done previously in the literature.

E. End effects

Aside from the aforementioned discussion, there was also a distinct three-dimensional effect contributing to the hydrodynamics of cases ii and iii: that of the free end effects on the flow.

It can be noted from Fig. 16 that the mean velocity vector field projected in the x -plane increased in magnitude on cross-sections passing through the bodies ($x/D = -0.4$ to 0.4), and it swirled around the free end, producing streamwise vortices whose axes were aligned with the x -direction, in the fashion of the upwash- or downwash-like effect. These vortices were barely noticeable in the first cross section, which just past P_1 , P'_1 , at $x/D = -0.4$. Still, as the flow went around the main body, $x/D = 0$, their formation became clearer. The same analysis is not shown here for the infinite bodies because this flow structure was not observed in such cases.

Between systems of finite length, the main difference was in the faster velocity field of case iii relative to that of case ii along the spanwise direction. The free surface, in blocking the flow that would, otherwise, be directed to one of the ends of the cylinder, sped up the flow in the spanwise z -direction, compared with the former case, as it can be appreciated in the row $x/D = 0.4$ of Fig. 16. This faster velocity field reached the ends of the main body and rods and led to stronger streamwise vortices and a more widespread wake, as presented by Fig. 15. Moreover, the figure also makes clear that the free water surface of case iii amounted to a more significant impact on the streamwise vortices, notably in the number of turbulent eddies with a high

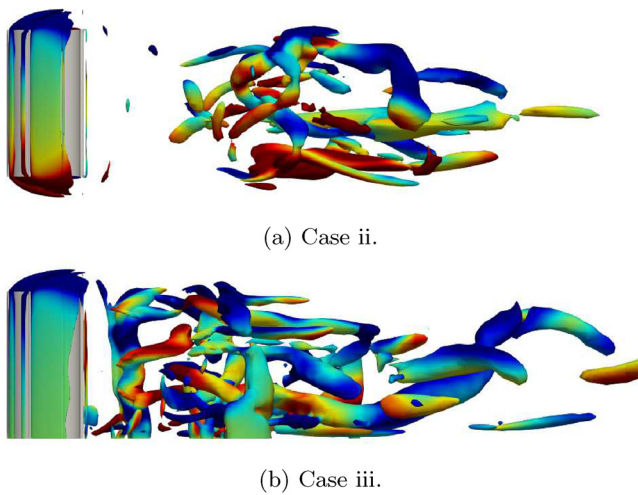


FIG. 15. Contours of dimensionless streamwise vorticity of cases ii (a) and iii (b), nondimensionalized by U_∞/D , ranging from -2.5 (blue) to 2.5 (red). Here, $Q = 2.5$. The represented cross section refers to the plane $y = 0$.

level of vorticity, represented by the presence of Q -contours in the entire wake region, further away into the wake (conversely, for case ii, Q -contours were restricted to a limited and rather intermediate region of the wake).

One of the effects of this three-dimensional phenomenon is how it affected the vortex formation length. Taking into consideration the contribution of Fox and West (1993), the separated flow that left the ends was responsible for delaying the interaction of the vortices and, thus, promoted greater formation length when compared with the respective bare cylinder cases since it led to a “less negative” base pressure. In turn, this culminated in the lower mean drag compared with infinitely long bodies.

Now, it must be acknowledged that between finite systems, in case ii, given sufficient distance away from the system, the vector field projected in the x -plane gradually disappeared, as it is progressively shown in Fig. 16 from $x/D = 0.0$ to $x/D = 1.0$, which is different behavior from that of case iii for the same x -stations: The planar slip-surface allowed streamwise vortices to prevail longer downstream. This is clearly in common with the paragraph above. Higher velocities along the span of the system (as observed for a single cylinder in Kawamura *et al.*, 1984) allowed streamwise vortices to persist long past the system. We further note that this effect was more accentuated for the entire system in comparison with the plain cylinder. This shows that the rods’ ends led to a build-up of the vortical effect that would, otherwise, occur for a single cylinder.

Another effect is related to the increase in lift from the bare cylinder to the entire system. When the rods were inserted around the main body, a greater pressure imbalance was established between the upper ($y/D > 0.5$) and the lower ($y/D < 0.5$) parts due to the formation of these trailing vortices. Recall from Figs. 9 and 10 that, in cases ii

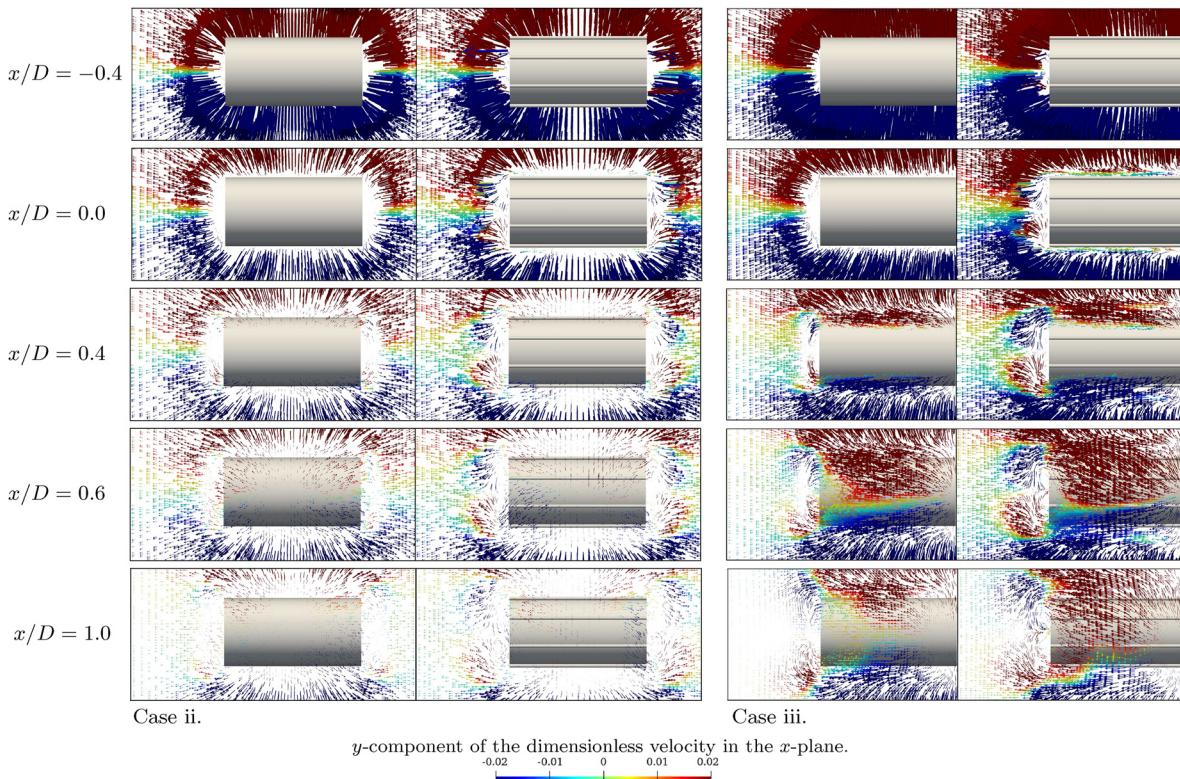


FIG. 16. Mean flow field over finite bodies projected in the yz plane at different stations x in the mean flow direction. Case iii presents a greater increment in upwash and downwash velocities due to the free ends of the cylinders.

and iii, the wake of the entire system demonstrated a more chaotic aspect and contained a greater diversity of turbulence scales. This is associated with the assertion by Kawamura *et al.* (1984) that the entire wake of low aspect ratio bodies corresponds with the interaction of trailing vortices in a region that span the entire length of the body (that would behave separately in bodies of high slenderness parameter L/D). Nonetheless, a noticeable feature can be observed from the videos (2D-view) provided in the [supplementary material](#) of this paper. The shear layer on one side of the system was partially convected away into the flow in the form of vortices, while the other part was mostly entrained into the wake and dissipated there, and a third very small parcel of one shear layer moved across the wake to cut off the other shear layer. As one of the major parts of the shear layer was dissipated within the wake, this may justify the greater lift as well because a larger region of low pressure was established above and below the entire system intermittently than it would if the contributions were similar to the usual mechanism exhibited in the work of Gerrard (1966).

Neither the absence of coherent vortex structures nor this form of entrainment recollects the typical Kármán vortex street, which is due to the lack of spanwise correlation and end effects. As such, vortex shedding broke away from the usual 2S shedding mode (Williamson and Roshko, 1988) and the part of the shear layer, entrained into the wake, was dissipated there due to viscous effects, leaving no contribution to the interaction and formation of the vortices. We further note that although these mechanisms added to the magnitude of the lift coefficient (from the plain cylinder to the entire system case), the collective effect was still weaker than that instigated by the correlation of case i, where end effects were neglected.

The lower correlation caused the formation of a wake for which spectral analysis did not provide a characteristic Strouhal number. This may also be the result of the low slenderness parameter used in this work, in common with Farivar (1981), as the author observed the appearance of more than one characteristic frequency for high aspect ratio cylinders but could not measure it for $L/D < 7.5$. The same applies here, for the bare cylinder and the entire system with $L/D = 2$. Thus, a lower level of organization in the wake directly associates with the flattening effect highlighted by the curves of Fig. 8. Indeed, the correlation induced by the assumption of a periodic condition to the ends of the body that was made in case i introduced an organizational effect on the wake that resulted in larger hydrodynamic coefficients and fluctuations.

As observed by Fröhlich and Rodi (2004), the resulting wake on a wall-mounted, plain cylinder deviates from a Kármán wake due to the bending and distortion of this well-correlated wake. This distinct behavior of the shear layer interaction with the body and with the wake draws attention to the extension to which an active mechanism of wake control, for example, spinning the rods, could have on vortex shedding of finite bodies of cases ii and iii and beyond, on end effects. An organizational effect has been widely observed for infinitely long cylinders in the literature (Assi *et al.*, 2018; 2019; Carvalho *et al.*, 2021), and it has drawn attention to optimization of systems involving peripheral rods as well (Fan *et al.*, 2020; Bingham *et al.*, 2018; Dehkordi *et al.*, 2018). Considering the dampening of the fluctuation of the hydrodynamic loads, it is an open question whether an active mechanism could be more efficient in low aspect ratio cylinders than in infinitely long ones.

V. CONCLUSION

Finite volume simulations under the turbulent formulation of detached-eddy simulations were conducted at $Re = 1000$. Validation, verification, and grid independence tests indicated a reliable numerical scheme for the computation of the flow about structures with free ends.

Three cases were verified: case i, where the cylinders followed a numerical scheme to simulate an infinitely long system; case ii, where end effects were considered in respect to both ends of the cylinders; and case iii, with one free end, while the other was attached to a slip-surface. Examination of the bare cylinder and of the entire system indicated that the free ends had a decreasing effect in the hydrodynamic loads greater than 40% in mean drag and over 92% in root mean square lift.

Despite the previous studies that ensure the incapacity of a passive mechanism to suppress vortex shedding at sufficiently high Reynolds numbers for infinitely long cylinders (Mittal and Raghuvanshi, 2001; Mittal and Kumar, 2003), the same study was not conducted for a system with free ends or with a free surface such as the present. To fit a circular cylinder with eight slender and passive wake-control rods under uniform flow at $Re = 1000$ proved insufficient to inhibit vortex shedding or to reduce the hydrodynamic loads compared with the plain body. Indeed, the greater obstruction to the flow caused by the surrounding slender bodies caused mean drag and root mean square lift to adopt higher values than those of the corresponding plain cylinder. Nevertheless, end effects promoted lower loads than those found in infinitely long bodies and were responsible for a formation length prolonged by at least 6.7% and weakening of vortex shedding in all cases. These features were shown to be the result of the more chaotic wake topology, which was also associated with end effects.

It was also exposed that the resulting wake was not of the Kármán type. Instead, a rather very small part of one shear layer was responsible for the cutoff of its opposite, and a major fraction of the shear layer was entrained and dissipated, contributing little to the interaction and formation of stronger vortices.

Streamwise vortices were detected in the time-averaged flow of the finite cases, and the absence of this flow structure was noted for infinite bodies. We have demonstrated that these vortices were enhanced cumulatively by the presence of the small rods and the slip-allowing surface (in connection with the increased velocity along the spanwise direction promoted by the blockage of the flow near the free surface).

Greater relevance of the frontal rods and negligible importance of the rear rods were observed in regard to individual contributions of the different rods comprising the passive mechanism, in contrast with Carvalho *et al.* (2021) and Carvalho and Assi (2022) for infinitely long bodies. The present results agree with and expand the knowledge of the previous works employing such a passive mechanism for infinitely long cylinders and pave the way for the application of this system to low aspect ratio structures under an active mechanism of wake control. For example, spinning the rods (Mittal, 2001; Korkischko and Meneghini, 2012) may be able to not only control vortex shedding and vortex-induced vibrations but also further step into the reorganization of the wake into a Kármán street, reduce hydrodynamic loads through, and even eliminate these phenomena entirely in bluff structures of finite length. These matters are left for future work.

SUPPLEMENTARY MATERIAL

See the [supplementary material](#) for videos of Q-contours (planar and 3D views) of cases i, ii, and iii.

ACKNOWLEDGMENTS

I.A.C. is grateful to CAPES Brazilian Ministry of Education for his Ph.D. scholarship and the National Laboratory for Scientific Computing (LNCC/MCTI, Brazil) for providing HPC resources of the SDumont supercomputer. G.R.S.A. acknowledges the support of FAPESP, Brazil (No. 2011/00205-6) and CNPq, Brazil (No. 306146/2019-3). We gratefully acknowledge the support of the RCGI Research Centre for Greenhouse Gas Innovation, hosted by the University of São Paulo, Brazil, and sponsored by FAPESP (No. 2020/15230-5) and Shell Brazil.

AUTHOR DECLARATIONS

Conflict of Interest

The authors have no conflicts to disclose.

Author Contributions

Icaro Amorim de Carvalho: Conceptualization (supporting); Data curation (lead); Formal analysis (equal); Investigation (equal); Methodology (equal); Software (lead); Validation (equal); Visualization (equal); Writing – original draft (lead); Writing – review & editing (equal). **Gustavo R. S. Assi:** Conceptualization (lead); Data curation (supporting); Formal analysis (equal); Funding acquisition (lead); Investigation (equal); Methodology (equal); Resources (lead); Software (supporting); Supervision (lead); Validation (equal); Visualization (equal); Writing – review & editing (equal).

DATA AVAILABILITY

The data that support the findings of this study are available from the corresponding author upon reasonable request.

REFERENCES

- Assi, G. R. S., Crespi, T., and Gharib, M., "Novel geometries of serrated helical strakes to suppress vortex-induced vibrations and reduce drag," *Appl. Ocean Res.* **120**, 103034 (2022).
- Assi, G. R. S., Orselli, R. M., and Silva-Ortega, M., "Suppression of vortex shedding with rotating wake-control cylinders: Numerical investigation at a moderate Reynolds number," in *International Conference on Offshore Mechanics and Arctic Engineering* (American Society of Mechanical Engineers, 2018), Vol. 51210.
- Assi, G. R. S., Orselli, R. M., and Silva-Ortega, M., "Control of vortex shedding from a circular cylinder surrounded by eight rotating wake-control cylinders at $Re = 100$," *J. Fluids Struct.* **89**, 13–24 (2019).
- Behr, M., Hastreiter, D., Mittal, S., and Tezduyar, T., "Incompressible flow past a circular cylinder: Dependence of the computed flow field on the location of the lateral boundaries," *Comput. Methods Appl. Mech. Eng.* **123**, 309–316 (1995).
- Behr, M., Liou, J., Shih, R., and Tezduyar, T., "Vorticity-streamfunction formulation of unsteady incompressible flow past a cylinder: Sensitivity of the computed flow field to the location of the outflow boundary," *Int. J. Numer. Methods Fluids* **12**, 323–342 (1991).
- Bingham, C., Raibaudo, C., Morton, C., and Martinuzzi, R., "Suppression of fluctuating lift on a cylinder via evolutionary algorithms: Control with interfering small cylinder," *Phys. Fluids* **30**, 127104 (2018).
- Carvalho, I. and Assi, G., "Enhanced control of the turbulent flow past a circular cylinder with rotating rods inspired by an inviscid solution," *J. Fluids Struct.* **113**, 103652 (2022).
- Carvalho, I. A., Assi, G. R. S., and Orselli, R. M., "Wake control of a circular cylinder with rotating rods: Numerical simulations for inviscid and viscous flows," *J. Fluids Struct.* **106**, 103385 (2021).
- Choi, H., Jeon, W.-P., and Kim, J., "Control of flow over a bluff body," *Annu. Rev. Fluid Mech.* **40**, 113–139 (2008).
- Dehkordi, E. K., Goodarzi, M., and Nourbakhsh, S., "Optimal active control of laminar flow over a circular cylinder using Taguchi and ANN," *Eur. J. Mech.-B* **67**, 104–115 (2018).
- Fan, D., Yang, L., Wang, Z., Triantafyllou, M. S., and Karniadakis, G. E., "Reinforcement learning for bluff body active flow control in experiments and simulations," *Proc. Natl. Acad. Sci. U. S. A.* **117**, 26091–26098 (2020).
- Farivar, D., "Turbulent uniform flow around cylinders of finite length," *AIAA J.* **19**, 275–281 (1981).
- Fox, T. A. and West, G., "Fluid-induced loading of cantilevered circular cylinders in a low-turbulence uniform flow. Part 1: Mean loading with aspect ratios in the range 4 to 30," *J. Fluids Struct.* **7**, 1–14 (1993).
- Franzini, G. R., Gonçalves, R. T., Meneghini, J. R., and Fujarra, A. L. C., "One and two degrees-of-freedom vortex-induced vibration experiments with yawed cylinders," *J. Fluids Struct.* **42**, 401–420 (2013).
- Fröhlich, J. and Rodi, W., "Les of the flow around a circular cylinder of finite height," *Int. J. Heat Fluid Flow* **25**, 537–548 (2004).
- Gerrard, J. H., "The mechanics of the formation region of vortices behind bluff bodies," *J. Fluid Mech.* **25**, 401–413 (1966).
- Goldstein, S., *Modern Developments in Fluid Dynamics* (1965), Vol. 2, p. 439.
- Gonçalves, R., Franzini, G., Rosetti, G. F., Meneghini, J., and Fujarra, A., "Flow around circular cylinders with very low aspect ratio," *J. Fluids Struct.* **54**, 122–141 (2015).
- Gonçalves, R. T., Meneghini, J. R., and Fujarra, A. L., "Vortex-induced vibration of floating circular cylinders with very low aspect ratio," *Ocean Eng.* **154**, 234–251 (2018).
- Kawamura, T., Hiwada, M., Hibino, T., Mabuchi, I., and Kumada, M., "Flow around a finite circular cylinder on a flat plate: Cylinder height greater than turbulent boundary layer thickness," *Bull. JSME* **27**, 2142–2151 (1984).
- Kim, S.-E. and Mohan, L. S., "Prediction of unsteady loading on a circular cylinder in high Reynolds number flows using large eddy simulation," in *International Conference on Offshore Mechanics and Arctic Engineering* (ASME, 2005), Vol. 41979, pp. 775–783.
- Korkischko, I. and Meneghini, J., "Suppression of vortex-induced vibration using moving surface boundary-layer control," *J. Fluids Struct.* **34**, 259–270 (2012).
- Luo, S., "Flow past a finite length circular cylinder," in *The Third International Offshore and Polar Engineering Conference* (OnePetro, 1993).
- Luo, S., Gan, T., and Chew, Y., "Uniform flow past one (or two in tandem) finite length circular cylinder(s)," *J. Wind Eng. Ind. Aerodyn.* **59**, 69–93 (1996).
- Mittal, S., "Control of flow past bluff bodies using rotating control cylinders," *J. Fluids Struct.* **15**, 291–326 (2001).
- Mittal, S. and Kumar, B., "Flow past a rotating cylinder," *J. Fluid Mech.* **476**, 303–334 (2003).
- Mittal, S. and Raghuvanshi, A., "Control of vortex shedding behind circular cylinder for flows at low Reynolds numbers," *Int. J. Numer. Methods Fluids* **35**, 421–447 (2001).
- Newman, J. N., *Marine Hydrodynamics* (The MIT Press, 2018).
- Norberg, C., "Flow around a circular cylinder: Aspects of fluctuating lift," *J. Fluids Struct.* **15**, 459–469 (2001).
- Patankar, S. V., *Numerical Heat Transfer and Fluid Flow* (Taylor & Francis, 1980).
- Saltara, F., Neto, A., Lopez, J. et al., "3D CFD simulation of vortex-induced vibration of cylinder," *Int. J. Offshore Polar Eng.* **21**, 1–6 (2011); available at https://www.researchgate.net/publication/289347277_3D_CFD_Simulation_of_Vortex-induced_Vibration_of_Cylinder.

- Silva-Ortega, M. and Assi, G. R. S., "Flow-induced vibration of a circular cylinder surrounded by two, four and eight wake-control cylinders," *Exp. Therm. Fluid Sci.* **85**, 354–362 (2017).
- Silva-Ortega, M. and Assi, G. R. S., "Hydrodynamic loads on a circular cylinder surrounded by two, four and eight wake-control cylinders," *Ocean Eng.* **153**, 345–352 (2018).
- Spalart, P. R., "Comments on the feasibility of les for wings, and on a hybrid rans/les approach," in *Proceedings of First AFOSR International Conference on DNS/LES* (Greyden Press, 1997).
- Spalart, P. and Allmaras, S., "A one-equation turbulence model for aerodynamic flows," in *30th Aerospace Sciences Meeting and Exhibit* (AIAA, 1992), p. 439.
- Spalart, P. R., Deck, S., Shur, M. L., Squires, K. D., Strelets, M. K., and Travin, A., "A new version of detached-eddy simulation, resistant to ambiguous grid densities," *Theor. Comput. Fluid Dyn.* **20**, 181–195 (2006).
- Strykowski, P. J. and Sreenivasan, K. R., "On the formation and suppression of vortex shedding at low Reynolds numbers," *J. Fluid Mech.* **218**, 71–107 (1990).
- Sumner, D., Heseltine, J., and Dansereau, O., "Wake structure of a finite circular cylinder of small aspect ratio," *Exp. Fluids* **37**, 720–730 (2004).
- Tennekes, H. and Lumley, J. L., *A First Course in Turbulence* (MIT Press, 1972).
- Wieselsberger, C., "New data on the laws of fluid resistance," Report No. NACA-TN-84, 1922.
- Williamson, C. H. K., "Vortex dynamics in the cylinder wake," *Annu. Rev. Fluid Mech.* **28**, 477–539 (1996).
- Williamson, C. H. and Roshko, A., "Vortex formation in the wake of an oscillating cylinder," *J. Fluids Struct.* **2**, 355–381 (1988).
- Zdravkovich, M. M., "Review and classification of various aerodynamic and hydrodynamic means for suppressing vortex shedding," *J. Wind Eng. Ind. Aerodyn.* **7**, 145–189 (1981).